



The exosomal secretomes of mesenchymal stem cells extracted via 3D-printed lithium-doped calcium silicate scaffolds promote osteochondral regeneration

Tsung-Li Lin^{a,b,c,1}, Yen-Hong Lin^{d,1}, Alvin Kai-Xing Lee^b, Ting-You Kuo^a, Cheng-Yu Chen^d, Kun-Hao Chen^e, Yun-Ting Chou^f, Yi-Wen Chen^{a,d,**}, Ming-You Shie^{g,h,i,*}

^a Graduate Institute of Biomedical Sciences, China Medical University, Taichung, 406040, Taiwan

^b Department of Orthopedics, China Medical University Hospital, Taichung, 404332, Taiwan

^c Department of Sports Medicine, College of Health Care, China Medical University, Taichung, 406040, Taiwan

^d x-Dimension Center for Medical Research and Translation, China Medical University Hospital, Taichung, 404332, Taiwan

^e School of Medicine, China Medical University, Taichung City, 406040, Taiwan

^f Graduate Institute of Dental Science and Oral Health Industries, China Medical University, Taichung, 406040, Taiwan

^g Department of Biomedical Engineering, China Medical University, Taichung, 406040, Taiwan

^h School of Dentistry, China Medical University, Taichung, 406040, Taiwan

ⁱ Department of Bioinformatics and Medical Engineering, Asia University, Taichung, 41354, Taiwan

ARTICLE INFO

Keywords:

Additive manufacture
3D scaffold
Osteochondral defect
Lithium
Calcium silicate
Exosomes

ABSTRACT

The development of surface modification techniques has brought about a major paradigm shift in the clinical applications of bone tissue regeneration. Biofabrication strategies enable the creation of scaffolds with specific microstructural environments and biological components. Lithium (Li) has been reported to exhibit anti-inflammatory, osteogenic, and chondrogenic properties by promoting several intracellular signaling pathways. Currently, research focuses on fabricating scaffolds with simultaneous dual bioactivities to enhance osteochondral regeneration. In this study, we modified the surface of calcium silicate (CS) scaffolds with Li using a simple immersion technique and evaluated their capabilities for bone regeneration. The results showed that Li ions could be easily coated onto the surfaces of CS scaffolds without affecting the microstructural properties of CS itself. Furthermore, the modifications did not affect the printing capabilities of the CS, and porous scaffolds could be fabricated via extrusion. Moreover, the presence of Li improved the surface roughness and hydrophilicity, thus leading to enhanced secretion of osteochondral-related regeneration factors, such as alkaline phosphatase (ALP), bone sialoprotein (BSP), and collagen II (Col II) proteins. Subsequent *in vivo* studies, including histological and micro-CT analyses, confirmed that the Li-modified CS scaffolds promoted osteochondral regeneration. The transcriptome analysis suggested that the enhanced osteochondrogenic capabilities of our scaffolds were influenced by paracrine exosomes. We hope this study will inspire further research on osteochondral regeneration.

1. Introduction

The regeneration and repair of articular cartilage lesions are some of the most challenging issues in orthopedics and sports medicine [1]. Articular cartilage lesions are regarded as a significant risk factor for osteoarthritis in young adults and adolescents owing to the presence and imbalance of macrophages in the cartilage [2]. Articular cartilage

lesions are commonly caused by trauma, surgical procedures, or chronic wear and tear. However, articular cartilage lacks vascularization and has a low cell density, thus contributing to its inability to self-regenerate and repair after injury [3]. Therefore, external approaches are required to enhance cartilage regeneration. Several surgical procedures, such as arthroplasty, chondral drilling, microfracturing, and mosaicplasty, attempt to induce cartilage regeneration in patients with articular

* Corresponding author. Department of Biomedical Engineering, China Medical University, Taichung, 406040, Taiwan.

** Corresponding author. Graduate Institute of Biomedical Sciences, China Medical University, Taichung, 406040, Taiwan.

E-mail addresses: evinchen@mail.cmu.edu.tw (Y.-W. Chen), eric@mail.cmu.edu.tw (M.-Y. Shie).

¹ These authors contributed equally to this work.

<https://doi.org/10.1016/j.mtbio.2023.100728>

Received 8 April 2023; Received in revised form 22 June 2023; Accepted 7 July 2023

Available online 19 July 2023

2590-0064/© 2023 Published by Elsevier Ltd. This is an open access article under the CC BY-NC-ND license (<http://creativecommons.org/licenses/by-nc-nd/4.0/>).

cartilage lesions. However, the effects of various surgical procedures are often limited as articular cartilage lesions often extend deep with the involvement of the subchondral bone tissues. Proper articular cartilage regeneration requires close interaction and communication between the cartilage and its underlying subchondral bone tissue [4]. Therefore, simultaneous regeneration of osteochondral tissue is critical for ensuring proper cartilage regeneration [5].

Tissue engineering, a tissue regenerative technology, encompasses cells, growth factors, and scaffolds, which act as a structural framework supports [6]. Recently, biofabrication strategies have evolved to enable the precise control of the microstructural environment and biological components of scaffolds [7–9]. Such capabilities are crucial for mimicking tissue interfaces, especially for osteochondral tissues, where the respective parts have unique architectural and structural frameworks and functions. Three-dimensional (3D) porous scaffolds with appropriate biodegradability are often used as matrix materials in tissue regeneration [10,11]. Numerous synthetic and natural biomaterials have been developed for this purpose, and calcium silicate (CS) is the most commonly used biomaterial for osteochondral regeneration [12, 13]. The capability of CS scaffolds to release both calcium and silicate ions into their surrounding fluids has been widely reported and is acknowledged to play a role in enhancing osteochondral regeneration. Trace elements of silicate in the human body are primarily found in the calcification sites of bones and are involved in the early stages of bone mineralization. In previous studies, silicate has been reported to significantly enhance the proliferation and expression of osteogenic- and chondrogenic-related genes and regeneration-related factors [14]. Moreover, silicate ions have been reported to modulate the expression of the cartilage extracellular matrix, thereby positively impacting cartilage regeneration [15]. Previously, multilayered scaffolds have been fabricated to mimic the microstructure of osteochondral tissues. However, it is technically difficult to imitate the physiological structure and function of the osteochondral tissue using multilayered scaffolds. Therefore, scientists are now attempting to fabricate scaffolds with simultaneous dual bioactivities to enhance osteochondral regeneration.

Lithium (Li) is a drug commonly used to treat depressive disorders and has recently been found to play a role in the treatment of arthritis [16]. In *in vitro* studies of mice with bone defects, it was reported that the presence of Li enhanced Wnt signaling molecules, which led to subsequent osteochondral formation and regeneration [17]. In addition, Li selectively inhibited macrophage phosphorylation, prevented cartilage degradation, induced chondrocyte proliferation, and enhanced the regenerative capability of chondrocytes [18]. Li has also been reported to promote chondrocyte maturation via the HIF pathway and enhance cartilage extracellular matrix protein secretion by enhancing SOX9, collagen II (Col II), aggrecan, and N-cadherin expression. Furthermore, cells also play an important role in tissue engineering studies. Mesenchymal stem cells (MSCs) are commonly used in *in vitro* studies on cartilage regeneration because of their ability to proliferate and differentiate [19]. Recently, the efficacy of MSC-based scaffolds in cartilage regeneration has been attributed to the secretion and action of paracrine exosomes. Exosomes are nano-sized vesicles of approximately 50–100 nm with bilipid membranes that are present in the secretomes of MSCs; they have been reported to have therapeutic effects on heart, liver, and skin regeneration [20]. Several studies have reported the use of exosomes for osteochondral regeneration, namely eukaryotic initiation factor-2 from osteoblasts, the exosomal miRNAs miR-214-3p and miR-23a-5p from osteoclasts, and miR-218 from osteocytes [21,22]. Exosomes play a key role in every stage of osteochondral regeneration [23]. However, the exact mechanism by which the scaffolds influence exosomes to induce osteochondral regeneration remains unknown.

In this study, we present a novel approach by fabricating the Li-containing calcium silicate (LiCS) scaffold for osteochondral regeneration. The incorporation of Li in the scaffold aims to improve its characteristics and enhance the secretion of regeneration-related proteins. Furthermore, in addition to its effects on osteogenic- and

osteochondrogenic-differentiation, we also investigate the influence of the LiCS scaffold on the secretion of exosomes by mesenchymal stem cells. These exosomes play a crucial role in mediating intercellular communication and can potentially enhance the regenerative process, which is indicative of the differentiation processes.

2. Materials and methods

2.1. Preparation of LiCS powder

First, 65 g of CaO (Sigma-Aldrich, St. Louis, MO, USA), 25 g of SiO₂ (Sigma-Aldrich), and 10 g of Al₂O₃ (Sigma-Aldrich) were mixed with 0, 5, and 10 g of Li₂O (Sigma-Aldrich) in a beaker and stirred with a metal stirrer before being transferred to an alumina crucible (SSA-T Saya series, Japan). The crucible was then placed into an oven with a gradual exponential increment of 10 °C per minute until 1400 °C, after which it was sintered for 2 h before letting it cool to room temperature. The sintered powder was then mixed with 100% alcohol and ball milled at 300 rpm for 8 h. Subsequently, the solution was transferred into a beaker and allowed to dehydrate at 100 °C for 12 h to let the alcohol evaporate. The LiCS powder was collected and stored for further use. Fig. 1 below shows a flowchart of the preparation process of the LiCS powder.

2.2. 3D-printed LiCS scaffolds

First, the LiCS powder was mixed with 100% alcohol and stirred using a magnetic stirrer at 180 rpm for 2 h. The solution was then placed in an ultrasonic oscillator and mixed for 30 min to allow the powder to be completely dissolved. LiCS powder was mixed with melted polycaprolactone (PCL) at a ratio of 50: 50. The PCL was first weighed and melted at 180 °C to form a transparent liquid. The melted PCL was slowly added to a LiCS solution and stirred until the alcohol completely evaporated. The dried paste was then placed into an oven at 100 °C for 12 h for complete evaporation of alcohol to obtain a printable paste. The paste was loaded into a syringe and extruded using a 3D GeSim Bioprinter (BioScaffolder 3.1, GeSIM, Grosserkmannsdorf, Germany) to form a scaffold. Distance between each strut was designed to be 500 μm apart, with 7 struts per layer, and each layer was placed 90° perpendicular to the bottom layer. The groups used in this study were labeled Li0, Li5, and Li10, with each symbol representing the concentration of Li modification.

2.3. Characteristics of the scaffolds

The scaffolds were first rinsed with 75% alcohol to clean the surfaces of the scaffolds. The scaffolds were then placed and secured onto a double-sided tape on the platform. An appropriate amount of conductive carbon gel was placed around the perimeter of the scaffold and left to dry in a lyophilization machine (FIRSTEK, Taiwan) for 48 h. This procedure was performed to completely dehydrate the scaffolds before image acquisition. Subsequently, the entire surfaces of the scaffold and platform were coated with gold to enhance conductivity during image acquisition. Images were captured using a thermal field emission scanning electron microscope (JEOL JSM-7800F; JEOL Ltd., Tokyo, Japan). Different magnifications were used to observe the appearance and pore and strut characteristics of the 3D-printed Li-containing CS scaffolds.

2.4. X-ray diffractometry of the scaffolds

X-ray diffraction (XRD) was performed using a high-resolution X-ray diffractometer (Bruker D8 SSS; Bruker Corporation, Karlsruhe, Germany) are directed at various ions and molecules, and the length of the reflected X-rays is in the visible spectrum. Compounds with different ionic compositions could be distinguished using XRD because different diffraction peaks were present owing to the different angles between the ionic bonds. The settings used in this study were: a scanning rate of 1°

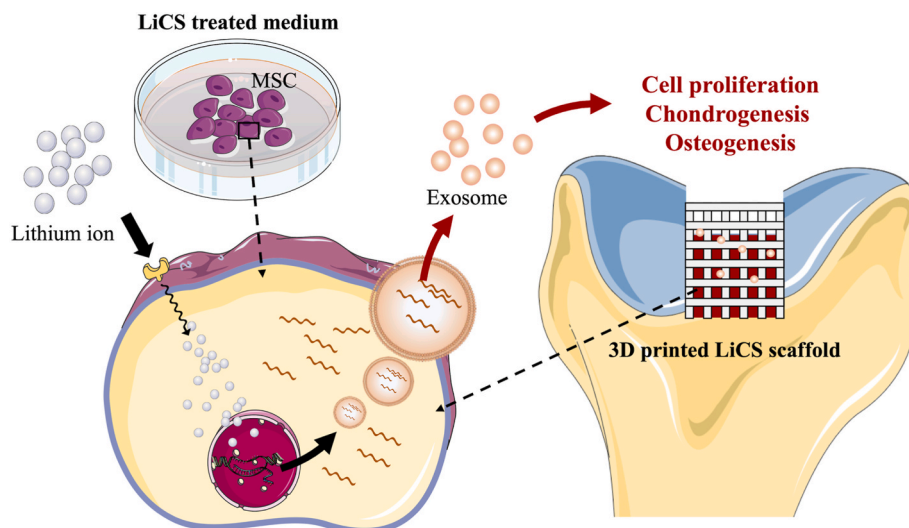


Fig. 1. Schematic diagram of implantation of 3D-printed LiCS scaffold and the release of exosomes affecting mesenchymal stem cells in cell proliferation, osteogenesis, and chondrogenesis.

per min and at a range of $2\theta = 20^{\circ}$ – 50° .

2.5. Hydrophilicity test

For the hydrophilicity tests, 10 μ L of deionized water was dripped onto the surfaces of various scaffolds, and a desktop microscope was used to capture images of the water droplets that landed on the scaffold. The images were processed using ImageJ software (National Institutes of Health, USA) to calculate the contact angle.

2.6. Mechanical testing

A mechanical testing machine (EZ-Test; Shimadzu Corp., Kyoto, Japan) was used to measure the mechanical strength of the scaffolds. A setting of 1 mm/min was used for the static compression test, and the results were plotted as stress-strain curves for analysis. The test was performed according to the ISO Standard 13314:2011 requirements for compressive and plateau stress tests.

2.7. Immersion test for hydroxyapatite formation

The LiCS scaffolds were prepared and placed in 75% alcohol with UV for sterilization. Sterile deionized water was then used to clean the scaffolds before immersing them into simulated body fluid (SBF) for 1, 2, 4, 12, and 18 weeks. Subsequently, the scaffolds were removed from the SBF, rinsed with deionized water, and placed into an incubator at 37 $^{\circ}$ C for 12 h to ensure complete dehydration. The scaffolds were prepared using protocols similar to those described above, and a scanning electron microscope was used to observe the formation of hydroxyapatite on the scaffolds.

2.8. Degradation appraisalment of the Li-containing CS scaffolds

Li0 and Li10 were weighed using an electronic weighing scale and disinfected by immersion in 75% alcohol, followed by UV irradiation. The scaffolds were then cleaned with sterile deionized water before immersion in SBF for 0.5, 1, 3, and 6 months. Subsequently, the scaffolds were removed from the SBF, rinsed with deionized water, and dried at 37 $^{\circ}$ C for 12 h to ensure complete dehydration. The weight of the dried scaffolds was recorded to assess their degradation rate. Finally, the released Ca, Si, and Li ions were analyzed by inductively coupled plasma-atomic emission spectrometry (PerkinElmer OPT 1 MA 3000DV; Shelton, CT, USA).

2.9. Cell culture

The Wharton's jelly mesenchymal stromal cells (WJMSCs) utilized in this study were purchased from Invitrogen (Invitrogen, Grand Island, NY, USA). The medium for WJMSCs contained 5% fetal bovine serum, 1% mesenchymal stem cell growth supplement, and 1% penicillin/streptomycin solution in mesenchymal stem cell medium (#7501, ScienCell Research Laboratories, Carlsbad, CA, USA). For the chondrocyte differentiation test, a chondrocyte differentiation basal medium with 10% chondrogenesis supplement was used. Cells (2×10^5 cells/mL) were cultured on each scaffold, and the control group used in this study was cultured on dishes. After cell seeding, the scaffolds were placed into an incubator at 37 $^{\circ}$ C with 5% CO₂. The medium was changed every two to three days or according to the cultural conditions.

2.10. Cell proliferation and morphology

After various time points, the scaffolds were removed, rinsed three times with phosphate-buffered saline (PBS), and mixed with PrestoBlue solution. The culture well was then placed in an incubator at 37 $^{\circ}$ C for 30 min. Subsequently, 100 μ L of the reactant solution was transferred to a 96-well microplate. A spectrophotometer (Infinite Pro M200; Tecan, Männedorf, Switzerland) was used to measure the absorbance at 570 nm, with a reference wavelength of 600 nm. Measurements were conducted in triplicate for quantitative analysis. In addition, the scaffolds were washed with PBS, fixed in 4% paraformaldehyde for 30 min, and then rinsed thrice with PBS; 0.1% Triton X-100 was also added for 10 min for cell membrane permeation. Alexa Fluor™ 488 Phalloidin with PBS (1:500; Invitrogen) was then added, and the mixture was shaken for 60 min in the dark. Next, DAPI (4',6-diamidino-2-phenylindole, 50 nM) was added, and the mixture was shaken for 30 min in the dark. Subsequently, the scaffolds were removed, washed with deionized water and PBS, and observed under a confocal microscope (Leica TCS SP8; Leica microsystems, Wetzlar, Germany). Furthermore, built-in software was used to observe and analyze images with varying depths.

2.11. Biocompatibility of LiCS scaffolds extracts

The indirect biocompatibility was investigated by following a revised version of ISO10993-5. First, we manufactured the 3d-printed LiCS scaffold, which was subsequently washed with PBS twice, followed by sterilization in 75% ethanol at room temperature in a laminar flow for 60 min. To get the extracts of these scaffolds, the different groups were

then soaked in Dulbecco's modified Eagle's Medium (DMEM) and placed in a 37 °C incubator with the settings of 75% humidity and 5% CO₂ for 24 h. Concurrently, WJMSC (10⁴ cells) were cultured in a 96-well at 37 °C for 24 h. Then, the medium was removed and replaced with 100 μL/well of the various scaffolds extract solution. After 1 day of cell culture, the extract solution was removed and replaced with PrestoBlue solution in each well. The analysis processing was similar to 2.10.

2.12. Inflammation assay

For the inflammation assay, WJMSC were cultured on the LiCS scaffold with mesenchymal stem cell medium for 1 day, the cell was lysis by NP40 and collected protein for analyzed the inflammation-related marker. The quantity of TNF-α (BMS223-4, Invitrogen), IL-1β (#BMS224-2, Invitrogen), and IL-10 (#BMS215HS, Invitrogen) was estimated by enzyme-linked immunosorbent assay according to the manufacturer's instructions. The concentrations of targeted protein in each sample were considered by comparing the absorbance with a standard curve.

2.13. Osteogenic differentiation assay

For the osteogenic assay, WJMSCs were cultured in osteogenesis assay kits (StemPro™ osteogenesis differentiation kit, Invitrogen) for 3, 7, and 14 d to estimate cell differentiation on different scaffolds. ALP activity and BSP and osteocalcin (OC) expression levels were assayed at different time points. For the ALP assay, the cells were lysed in 100 μL of 1% NP40 Buffer (NP40 Cell Lysis Buffer, Invitrogen), and a pNPP ALP assay kit (BioAssay Systems, Biocore, NSW, Australia) was used for determination. Total protein content was measured using a BCA protein detection kit (Invitrogen). Relative ALP activity was calculated as the change in absorbance divided by the total protein content. In addition to the above methods, BSP (MBS261861; MyBioSource, San Diego, CA, USA) and OC (#KAQ1381; Invitrogen) were analyzed using an enzyme-linked immunosorbent assay (ELISA) kit after 7 and 14 d of culture. The ELISA kit was used according to the manufacturer's instructions. Briefly, 50 μL of each sample was added to a well pre-coated with a specific antibody. The plate was then incubated for 1 h at room temperature, followed by the addition of a biotin-conjugated detection antibody and a streptavidin-HRP conjugate. The plate was incubated for 1 h at room temperature and then washed. Finally, the substrate solution was added, and the plate was incubated for 30 min in the dark. The reaction was stopped by adding stop solution and the absorbance was measured at 450 nm using a microplate reader. The concentrations of BSP and OC in each sample were determined by comparing the absorbance with a standard curve.

2.14. Mineralization

After 7 and 14 d of culture, the scaffolds were removed, rinsed thrice with PBS, and fixed with 4% paraformaldehyde for 30 min. Next, the scaffolds were rinsed thrice with PBS, and soak in 0.5% Alizarin Red S solution on a shaker for 20 min. The scaffolds were then rinsed with deionized water and left to dry in an incubator. A BX53 Olympus fluorescence microscope (Olympus, Tokyo, Japan) set at 200 × magnification was used to detect the appropriate staining.

2.15. Chondrogenic differentiation assay

For the chondrogenesis assay, WJMSCs were cultured in osteogenesis assay kits (StemPro™ chondrogenesis differentiation kit; Invitrogen) for 3, 7, and 14 d to estimate cell differentiation on different scaffolds. At each designated time point, the scaffolds with cells were lysed for quantitative analysis of Col I (MBS7607063; MyBioSource), Col II (MBS263555; MyBioSource), and glycosaminoglycan (GAG, MBS7606393; MyBioSource) using ELISA. The test was performed three

times, and the results were averaged.

2.16. Animal studies

New Zealand male white rabbits weighing approximately 1.8 kg on average were obtained from the Animal Experiment Center at China Medical University (CMUIACUC-2020-034). First, the animals were secured and an anesthesia machine was used to deliver 5% isoflurane with oxygen for anesthesia. After the animals were sedated, the gas composition ratio was decreased to between 1.5 and 3.5%. An incision was made using a scalpel along the medial thigh to the knee, and the femur was exposed. A cylindrical hole with a diameter of approximately 4 mm and a depth of 8 mm was drilled onto the condyle, and various scaffolds were then implanted. The size of the hard-tissue scaffold was 6 mm (diameter) × 6.2 mm (height). The animals were sacrificed via CO₂ asphyxiation at the fourth and eighth weeks after implantation for subsequent analyses.

2.17. Micro-computed tomography (CT) and histological analysis

The micro-CT images of the scaffold-implanted regions were scanned using a multi-scale X-ray nano-CT system (SkyScan 2211; Bruker, Belgium) at a voltage of 100 kVp, 330 μA current, and output of 20 W. Images were reconstructed using reconstruction software (Insta Recon; Bruker, Belgium). Avizo 8.0 software (Visualization Sciences Group, France) was used to analyze bone volume fraction (BV/TV) and trabecular thickness (Tb.Th). After the micro-CT scan was completed, the sections were divided into sections of appropriate thickness using the freeze-section procedure. The sections were stained with hematoxylin and eosin (HE), the cartilage was stained with sulfated GAGs using Alcian blue (AB) stain, the collagen fibrils were stained using Masson's trichrome (MT) stain, and the calcified bone was stained dark red with Von Kossa (VK) staining. Finally, the samples were examined under an optical microscope.

2.18. Fabrication and characterization of WJMSC-derived exosome

WJMSC were cultured on Li0, Li5, and Li10 scaffolds in DMEM supplemented with exosome-depleted FBS (Invitrogen). After 3 d, the medium was centrifuged at 2000×g for 15 min to remove cellular debris and filtered with 0.22 μm filter paper. Subsequently, the supernatant was concentrated by ultrafiltration (Amicon Ultra, 30 kDa; Merck Millipore, Billerica, MA, USA) at 5000×g for 8 min. The collected supernatant was subjected to tangential flow filtration (MAP.03-plus TFF System; Lefo Science, Taipei, Taiwan) and then filtered through membranes with a 300 kDa molecular weight cut-off. All exosomes were resuspended in PBS and stored at 4 °C for immediate use or stored at -80 °C for further use. First, exosomes were lysed in 100 μL of 1% NP40 Buffer (NP40 Cell Lysis Buffer). The total protein content of different exosomes was measured using a BCA protein assay kit. The extracted total protein (30 μg) was subjected to sodium dodecyl sulfate-polyacrylamide gel electrophoresis and transferred to a polyvinylidene difluoride (PVDF), after which the PVDF membrane was placed in a blocking buffer containing 5% bovine serum albumin for 1 h. Primary antibodies including CD63 (ab239686, Abcam, Cambridge, MA, USA), CD9 (ab239685, Abcam), Alix (ab88743, Abcam), HSP70 (ab47454, Abcam), TSG101 (ab125011, Abcam), and β-actin (A5441, Sigma-Aldrich) were added, and the mixtures were shaken overnight at 4 °C. Subsequently, the secondary antibodies diluted in TBST were shaken at room temperature for 1 h to visualize chemiluminescence. Protein expression was visualized on a PVDF membrane using an ECL kit (Merck Millipore) and quantified using ImageJ software (National Institutes of Health). The exosomes were fixed with 1% glutaraldehyde at 4 °C overnight. After washing off the solution and negatively staining with aqueous phosphotungstic acid for 1 min, the exosomes were laid onto Formvar carbon-coated grids to observe their ultrastructure using a

transmission electron microscopy (TEM) (JEOL JEM-1400; JEOL Ltd.). Exosomes were assayed using nanoparticle tracking analysis (NTA) (ZetaView®; Particle Metrix GmbH, Meerbusch, Germany). Their membranes were labeled with specific fluorescent makers, then injected into ZetaView® which analyzes the size distribution and concentration by calculating the Brownian motion of the molecules.

2.19. Uptake of exosomes

The exosomes (10^{10} exosomes/mL) were resuspended in 1 mL of PBS and sequentially mixed with a PKH67 fluorescent dye (Sigma-Aldrich) solution for 10 min. The mixture was then centrifuged at $50,000\times g$ for 10 min, and the supernatant was aspirated. The pellet was added to 10 mL PBS and centrifuged at $50,000\times g$ for 10 min. The supernatant with excess dye was removed, and the PKH26-labeled exosomes were resuspended in the culture medium. The WJMSCs were cultured to 60% in μ -slide wells for 24 h, and then the medium was replaced with WJMSC medium containing PKH67-labeled exosomes (5×10^9 exosomes/mL). After being incubated for 24 h, the cells were washed twice with PBS, fixed with 4% paraformaldehyde, and stained with DAPI and Alexa Fluor™ 488 Phalloidin with PBS (1:500, Invitrogen). After washing, a confocal fluorescence microscope was used to observe whether LiCS stimulated exosome uptake by WJMSC.

2.20. RNA sequencing analysis

Total RNA was extracted from clinical tissue samples, tissue-derived cells, and tissue-derived spheroids using a NucleoSpin® RNA Kit (Macherey-Nagel GmbH, Düren, Germany) according to the manufacturer's instructions. The quality, quantity, and integrity of the extracted RNA were evaluated using a NanoDrop1000 spectrophotometer and Agilent 2100 Bioanalyzer (Agilent Technologies, Santa Clara, CA, USA). Samples with RNA integrity (RIN) > 8.0 were used for RNA-seq. An mRNA-focused barcoded library was generated using the TruSeq Stranded mRNA Library Preparation Kit (Illumina, San Diego, CA, USA). The libraries were sequenced on the Illumina Nova Seq 6000 platform (Illumina) using 2×151 bp paired-end sequencing flow cells according to the manufacturer's instructions. The sequencing data were filtered using SOAPnuke, and a heatmap was drawn using Pheatmap (v1.0.8) according to the gene expression of different samples. Differential expression analysis was performed using DESeq2 (v1.4.5) with a Q value ≤ 0.05 . KEGG and GO enrichment analyses of annotated differentially expressed genes were performed using Phyper based on the hypergeometric test. Significant levels of terms and pathways were corrected by the Q value with a rigorous threshold (Q value ≤ 0.05)

using Bonferroni correction.

2.21. Statistical analyses

One-way statistical analysis of variance (ANOVA) was used to analyze the significance of between-group differences in each experiment. Scheffé's multiple comparison tests were performed to determine the significant deviations of each sample. Statistical significance was set at $p < 0.05$.

3. Results and discussion

3.1. Characterization of 3D-printed LiCS scaffolds

Photographs of the fabricated LiCS scaffolds are shown in Fig. 2A. All the scaffolds had highly specific and controlled macropores with pore sizes of approximately 500 μm . In addition, the scaffolds could be printed in up to 10 layers without any instances of structural weakness or collapse. Porous scaffolds have always been the center of attraction for bone tissue engineering, as such designs enable scaffolds to have a larger surface area, which is beneficial for hard tissue regeneration and integration with native tissues. Numerous reports have evaluated the optimal pore sizes for bone tissue regeneration, estimated to be within the range of 300–500 μm . Another important factor to consider for macroporous scaffolds is the interconnectivity between pores. The presence of interconnectivity allowed for initial cell adhesion and attachment in addition to initial tissue ingrowth into the center of the scaffolds [24]. Interconnectivity and increased surface areas allow more factors and proteins to be attached, thereby enhancing subsequent tissue regeneration. High-magnification images confirmed that the addition of Li did not affect the structural stability, interconnectivity, or macroporous structure of the scaffolds. In addition, the 3D-printed scaffolds and struts had regular, well-defined, and uniform pore distributions [25]. In addition, our past studies have also confirmed that the CS powder can be uniformly distributed throughout the scaffold, indicating the successful integration of CS powder and PCL [8]. This uniform dispersion is critical to ensure the mechanical integrity and performance of the scaffold, as it facilitates efficient load transfer and provides structural stability.

The water-in-air contact angles on the various scaffolds were evaluated using ImageJ software, as shown in Fig. 2B. The contact angle represents the wettability of the surfaces and indicates the degree of hydrophilicity of the scaffolds. A contact angle above 90° indicates that the biomaterial is hydrophobic and thus is not optimal for cell adhesion and attachment [26]. In the Li0 group, the contact angle was $83.2 \pm 2.8^\circ$

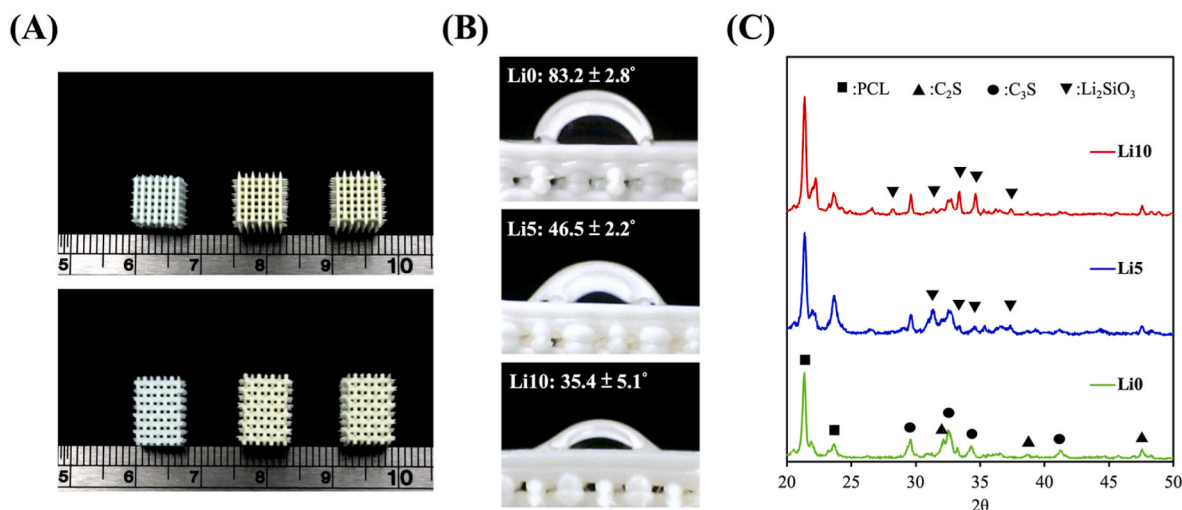


Fig. 2. (A) Appearance, (B) hydrophilicity, and (C) XRD pattern of LiCS scaffolds with different Li doping concentrations.

and the values gradually decreased with the addition of Li, with Li5 and Li10 having a contact angle of $46.5 \pm 2.2^\circ$ and $35.4 \pm 5.1^\circ$, respectively. A lower water contact angle indicates improved hydrophilicity, making LiCS scaffolds a better platform for initial cellular adhesion. This trend is similar to that reported by Li et al., in which the addition of Li improved the hydrophilicity of the scaffolds [27].

The compositions of various LiCS powders and scaffolds were evaluated using XRD (Fig. 2C). The analysis was performed on both the powder form and the scaffold as PCL was added prior to printing to provide printing stability support to LiCS. All groups exhibited the

characteristic peaks of Ca_2SiO_4 ($2\theta = 21.9^\circ, 29.6^\circ, 32.7^\circ, 36.6^\circ$, and 47.6°) and Ca_3SiO_5 ($2\theta = 31.2^\circ$ and 34.2°) [28]. In addition, Li-related peaks (Li_2SiO_3) were only present in Li5 and Li10 at $2\theta = 28.3^\circ, 31.4^\circ, 33.4^\circ, 34.7^\circ$, and 37.4° . This result indicates that Li was successfully incorporated into the CS scaffolds without affecting their original structural integrity. This is an important point to note, as we would like to consider both the characteristics of CS and the benefits of Li. Further XRD analysis of the CS/PCL scaffold revealed that PCL was successfully incorporated, with the PCL characteristic peak present at $2\theta = 21.0^\circ$. Furthermore, even with the addition of PCL, the characteristic peaks of

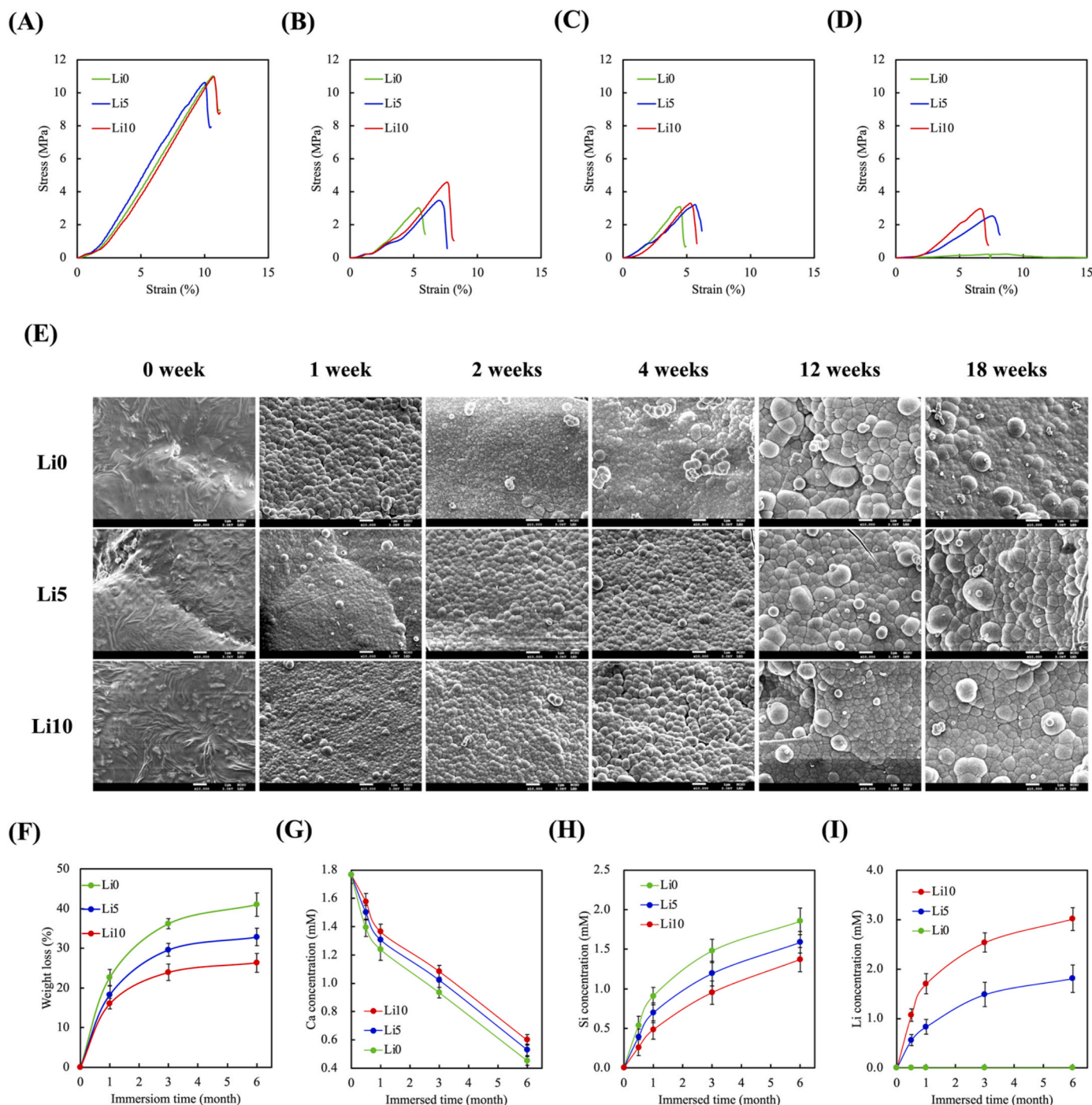


Fig. 3. Stress-strain curves, SEM surface morphology, weight loss, and ion release profiles of LiCS scaffolds after different immersion time points. (A) Stress-strain curves of the scaffolds after immersion at 0 months, (B) 1 month, (C) 3 months, and (D) 6 months. (E) Surface morphology of the scaffolds after immersion at different time points. (F) *In vitro* weight loss degradation of the scaffolds. (G) The release profile of Ca, (H) Si, and (I) Li ions from the scaffolds after immersion in simulated body fluid for 1 month.

CS and Li were still present in all groups, indicating that the addition of PCL did not affect the structural integrity of the LiCS scaffolds.

3.2. The mechanical properties and degradation of the LiCS scaffold

The mechanical characteristics of the various scaffolds over 6 months of immersion were evaluated and presented as stress-strain curves and weight loss, as shown in Fig. 3. A suitable scaffold for osteochondral regeneration should provide ample and sustained mechanical support. At month 0, no significant differences existed between the compressive strengths and compressive moduli of any of the scaffolds. The compressive strength of the scaffolds was well within the range of 10.5 ± 1.2 to 11.0 ± 0.9 MPa and the compressive strength of the scaffolds increased linearly with the deformation of the scaffolds (Fig. 3A). The compressive strength of our scaffolds was comparable with that of cancellous bone (2–12 MPa), indicating that the scaffolds could provide initial support and stability for osteochondral regeneration [29]. Furthermore, macroporous scaffolds have poor mechanical properties and low load-bearing capability due to their porosity [30]. However, in our study, even with proper pore sizes and porosity, we were still able to fabricate 3D-printed scaffolds with sufficient mechanical properties for osteochondral regeneration [31]. A good scaffold should provide sufficient mechanical support throughout the regeneration period. As seen from our results, Li0 had a residual mechanical strength of 2.8 ± 0.3 , 3.1 ± 1.1 , and 0.2 ± 0.05 MPa after 1 month (Fig. 3B), months (Fig. 3C), and 6 months (Fig. 3D) of immersion, respectively, whereas Li10 had a residual mechanical strength of 4.5 ± 1.4 , 3.3 ± 1.2 , and 2.9 ± 1.1 MPa, respectively. The residual mechanical strength of Li5 ranged between those of Li0 and Li10, indicating that we could further fine-tune and tailor our scaffolds according to their clinical regenerative requirements. It was also hypothesized that the addition of Li provided more ionic and covalent bonds within the scaffolds, thereby increasing their overall stability and slowing degradation [12]. This result provides the foundation for further *in vivo* studies, as it demonstrates that osteochondral defect healing could be enhanced only if the LiCS scaffold is implanted after the defects appear [32].

SEM images of the various scaffolds at different time points after SBF immersion are shown in Fig. 3E. At day 0, it could be seen that the surfaces of Li0 were generally smooth except for few irregular contours present. In contrast, Li5 and Li10 had rough and irregular surfaces, which improved early cellular adhesion and attachment. Rough surfaces increase fibrin entrapment, thus enhancing the adhesion of osteogenesis-related cells and improving the mechanical stability of the scaffolds after transplantation [33]. Furthermore, there was a positive correlation between the quality of initial cellular adhesion and subsequent cellular behaviors such as proliferation, differentiation, and protein secretion. After 3 d of immersion, spherical apatite clusters were seen deposited on the surfaces of the scaffolds, with Li10 having larger aggregates (approximately an average of 5–10 μm per aggregate) at all time points as compared with the rest of the groups. Furthermore, Li10 had a larger surface area for apatite formation than Li0 and Li5. CS is known to release calcium and silicon ions into its surrounding fluids, which are critical for apatite mineralization. The formation of a silicon layer on the surface of the scaffold provided a suitable nuclear attachment site for subsequent apatite formation. Li was hypothesized to increase apatite formation compared with silicon ions because of its smaller ionic radius and ionic placement when incorporated into CS [34]. The increased apatite formation on the surfaces of the scaffolds played an important role in enhancing osteoblast differentiation and proliferation, thereby enhancing the osteogenic capabilities of the scaffolds. Numerous studies have used the level of apatite formation as a predictor of the subsequent osteogenic capabilities of biomaterials.

The biodegradation rate of the bone graft is a critical factor that can affect the bone regeneration processing. In this study, the biodegradation behavior of LiCS scaffolds was examined by immersing the scaffolds in SBF for up to 6 months. Fig. 3F shows that increasing soaking time

continuously increased the weight loss of all scaffolds, which then gradually stabilized after 3 months. Upon the ions release profile, increased Li doping of CS led to a gradual decrease in the release of Ca ions during the immersion period (Fig. 3G). After immersion for 6 months, the Si concentrations of SBF were approximately 1.85 ± 0.17 mM, 1.59 ± 0.14 mM, and 1.37 ± 0.15 mM for Li0, Li5, and Li10, respectively (Fig. 3H). Other important factors support in observing the silicon ion release profiles, which could be related to the tissue regeneration rate [35]. In addition, Shie et al. demonstrated that the presence of silicon ions alone activated the osteogenic differentiation of osteoblasts in the absence of osteogenesis-inducing factors [15]. Fig. 3I shows that the Li5 and Li10 scaffolds exhibited a rapid increase in Li concentration within 1 month and then maintained a steady increase with increasing immersion time up to 6 months. In a prior study, Liu et al. confirmed that a culture medium with a Li-ion concentration of less than $14.56 \mu\text{g}/\text{mL}$ did not display cytotoxicity [36]. Our results showed that the maximum amount of Li ions released from the Li10 scaffolds after immersion in SBF for 14 d resulted in a cumulative maximum of $2.0 \mu\text{M}$, supporting the conclusion that the LiCS scaffolds fabricated in this study did not exhibit cytotoxicity [37].

3.3. Cell proliferation and morphology of WJMSCs cultured on LiCS scaffolds

The proliferation and morphology of WJMSCs cultured on the scaffolds were evaluated, as shown in (Fig. 4). All the scaffolds displayed a time-dependent increase in cellular proliferation (Fig. 4A). However, our results showed significantly higher cellular proliferation in the Li10 scaffolds after 1 d of culture than in the Li0 scaffolds ($p < 0.05$). Furthermore, Li5 had significantly higher cellular proliferation after 3 d of culture than the Li0 scaffolds. On day 14 of culture, Li10 and Li5 showed approximately 25% and 20% higher cellular proliferation, respectively, compared with Li0. From the F-actin and nuclear staining results, it was noted that there were more cells in the Li5 and Li10 groups, as seen from the increased surface areas covered by immunofluorescence staining (Fig. 4B). Most importantly, it was found that the MSCs were well-adhered on the surfaces of the scaffolds as seen from their spreading and well-defined F-actin microfilaments. Furthermore, to ensure the biocompatibility of the scaffold, we conducted an analysis of the scaffold extract following the ISO10993-5 specification (Fig. 4C). The findings conclusively indicated the non-toxic nature of the scaffold material, with the Li10 scaffold extract exhibiting a higher cell count compared to the Ctl, Li0, and Li5 scaffolds ($p < 0.05$). This result is consistent with the hydrophilicity results. Li et al. found that 30 and 50 ppm of Li ions significantly improved the osteogenic differentiation of MC3T3-E1 cells [38]. It is clear that Li improves cell behavior by inhibiting GSK3 β and therefore protecting β -catenin from degradation and resulting in the β -catenin signaling activation [39]. Furthermore, Li has been reported to activate and upregulate the RUNX2 gene, which encodes a transcription factor involved in the differentiation and maturation of osteoblasts [40]. In addition, we considered the general markers, such as TNF- α , IL-1 β , and IL-10 which were useful to identify inflammatory response [41]. As can see, the inflammation cytokine TNF- α and IL-1 was significantly reduced in the Li10 scaffold than Ctl, Li0, and Li5 ($p < 0.05$). In addition, we also investigated the anti-inflammation cytokine IL-10 to demonstrate LiCS could be an anti-inflammatory role in this study. IL-10 showed superior expression in Li10 is significantly higher than other scaffolds ($p < 0.05$). Therefore, further studies are required to confirm the dual functional capabilities of LiCS scaffolds in promoting osteochondral regeneration.

3.4. Osteogenesis- and chondrogenic-related protein expression

The expression levels of ALP, BSP, and OC in the scaffolds are shown in Fig. 5. Initially, all groups of scaffolds showed insignificant differences in ALP activity after 3 d of culture. However, after 7 d of culture,

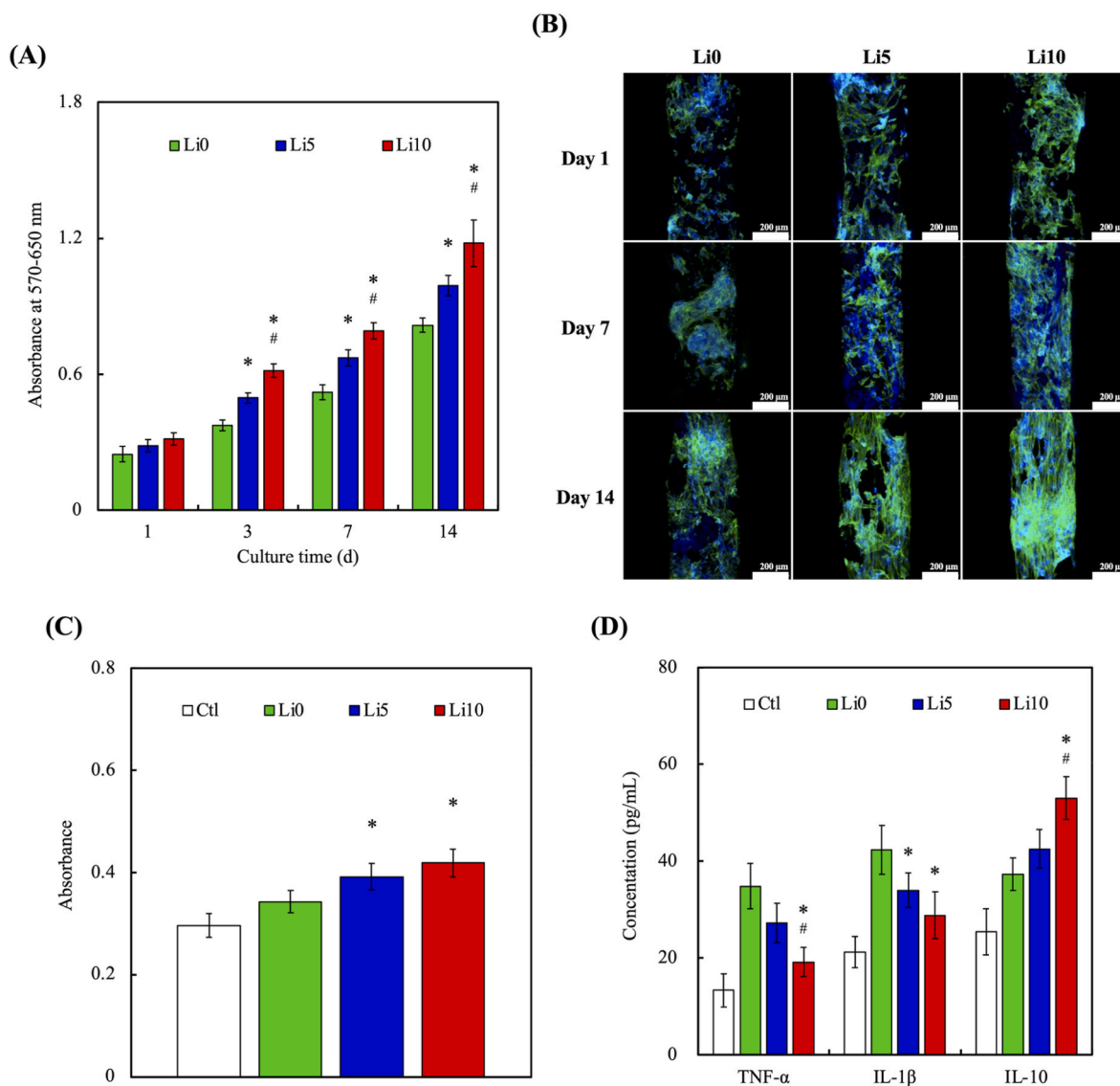


Fig. 4. (A) The proliferation of the WJMSC cultured in scaffolds for 1, 3, 7, and 14 d. (B) The cytoskeleton for F-actin filament staining of WJMSC cultured on scaffolds for 1, 3, and 7 d. The scale bar of the photograph is 200 μm. (C) The biocompatibility of WJMSCs cultured on the extracts from scaffolds for 1 day. (D) TNF-α, IL-1β, and IL-10 expression of WJMSC cultured in scaffolds for 1 day. * indicates a significant difference ($p < 0.05$) when compared with Li0, # indicates a significant difference ($p < 0.05$) when compared with Li5.

ALP levels in Li10 were 1.3-fold higher than those in Li0, which further increased to 3-fold after 14 d of culture (Fig. 5A). In the case of Li5, no significant difference in ALP activity was noted after 3 and 7 d of culture compared with Li0. Nevertheless, the difference became evident after 14 d of culture, and the ALP levels in Li5 were 2-fold higher than those in Li0. In addition, BSP (Fig. 5B) and OC (Fig. 5C) concentrations were also evaluated, and significantly higher levels were noted after both 7 and 14 d of culture compared with those of Li0. Although Li5 did not show a significant increase in BSP concentration on days 7 and 14 of culture compared with Li0, an increasing pattern of BSP was still noted with increasing concentrations of Li in the scaffolds. Pan et al. indicated that the mRNA expressions of ALP and OCN expression enhanced accordingly when the Li-ion concentration increased from 0.23 ppm to 7.42 ppm [41]. Taken together, it could be seen that Li enhanced both *in vitro* early and late osteogenic markers and thus has the potential for *in vivo* osteochondral regeneration. Alizarin Red S staining for calcium deposition was used to evaluate the terminal mineralization of the osteogenic differentiation of WJMSCs after 7 and 14 d of culture, as shown in Fig. 5D. Visually, it could be noted that there were scanty calcium

depositions on the surfaces of all the scaffolds after 7 d of culture, and there were no major differences in the staining intensity. However, after 14 d of culture, it was clear that Li5 and Li10 had higher amounts of calcium deposition, as indicated by the dark pink staining on the surfaces of the scaffolds. The ALP activity was enhanced, indicating that the LiCS scaffolds could release certain factors and stimulate osteogenic differentiation. In the late stages of osteogenesis, bone matrix mineralization is a symptom of bone maturation. Mineralization staining demonstrated that the LiCS scaffolds enhanced the number of calcium nodules, indicating the promotion of bone matrix mineralization. In addition, important osteogenesis-related secreted protein levels (ALP, BSP, and OC) were upregulated in Li10. These results strongly confirm that LiCS scaffolds might benefit *in vitro* osteogenic differentiation and lay the foundation for subsequent *in vivo* studies [42].

The concentrations of Col I (Fig. 5E), Col II (Fig. 5F), GAG (Fig. 5G), and Col II/Col I ratios (Fig. 5H) were also evaluated. A time- and concentration-dependent increase in all proteins was noted in all groups, with a significant increase in Col II and GAG secretion over the 14 d of culture. No statistically significant differences were observed in Col I

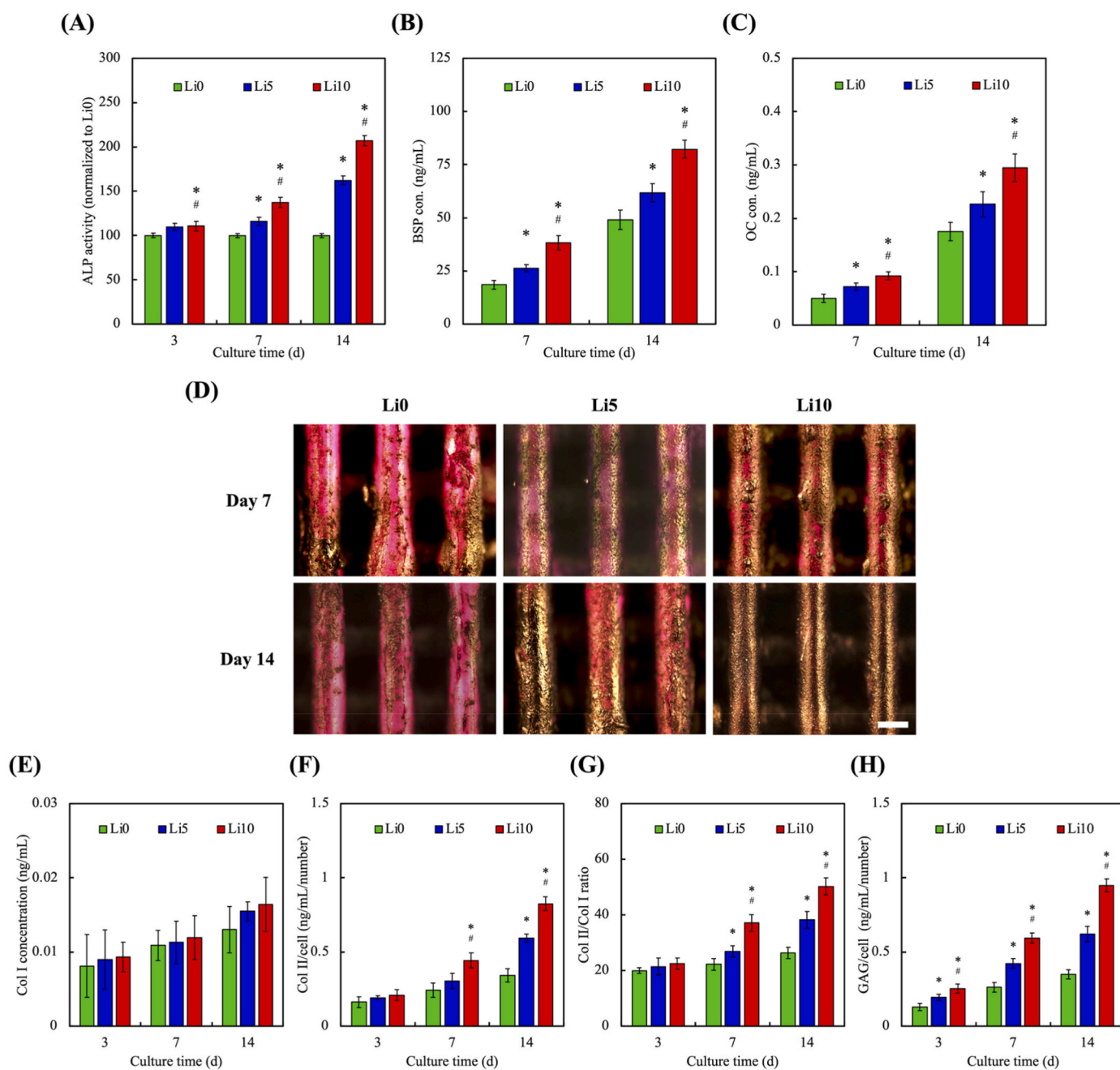


Fig. 5. The relevant indicators of osteogenic and chondrogenic changes observed in WJMSC cultured on LiCS scaffolds over different time points. Osteogenesis in early and late stages markers of (A) ALP expression of WJMSC for 3, 7 and 14 days, and (B) BSP, and (C) OC expression of WJMSC for 7 and 14 days. (D) Alizarin Red S staining of WJMSC to assess calcium mineral deposits after being cultured on scaffolds for 7 and 14 days. (E) Col I concentrations, (F) Col II concentrations, (G) Col II/Col I ratio, and (H) GAG concentrations of Li0, Li5, and Li10 after 3, 7, and 14 days of culture.

secretion between groups at any time point. However, Li10 had significantly higher levels of Col II and GAG on days 7 and 14 of culture ($1.4 \times$ and $2.2 \times$ for Col II, and $2.4 \times$ and $3.5 \times$ for GAG, respectively) as compared with those of Li0. In addition, Li10 also had significantly higher levels of Col II and GAG as compared with those of Li5 at all time points. This was further confirmed using the Col I/II ratio, where Li10 had $1.4 \times$ and $1.6 \times$ higher ratios than those of Li5 at all time points. Therefore, our results indicated that the presence of Li in CS scaffolds increased the time-dependent secretion of all osteogenic-related proteins, with Col II and GAG showing significant increases compared with Col I. As mentioned, collagen is the most abundant structural macromolecule in cartilage, with Col II representing 90–95% of the collagen extracellular matrix. These collagen molecules, together with other

minority subtypes, can interlink to form fibrils and fibers with proteoglycan aggregates such as GAG. Our results indicated that there was a significant increase in Col II and GAG secretion according to the Li concentration. These results show that the presence of Li specifically increased the expression of chondrogenesis-related proteins. According to Liu et al., the addition of Li into scaffolds improved chondrogenesis by upregulating exosome miR-455-3p, which then led to the suppression of histone deacetylase and subsequently enhanced histone H3 acetylation of chondrocytes [36]. They isolated miR-455-3p and cultured these exosomes with stem cells, which showed a similar enhancement in chondrogenesis. Furthermore, Li shields articular cartilage against degradation during osteoarthritis, via the inhibition of major signaling pathways involved in the pathological processes of osteoarthritis, such

as NF- κ B, p38 MAPK, and STAT-3 [43]. Taken together, it can be concluded that Li could be used to enhance chondrogenesis, and that the incorporation of Li into CS scaffolds could further upregulate the chondrogenic capabilities of CS scaffolds.

3.5. *In vivo* bone regeneration

Micro-CT was performed 8 and 12 weeks after LiCS scaffold implantation, as shown in (Fig. 6A). The BV/TV and Tb.Th ratios were also calculated and are presented in Fig. 6B and C. BV is the volume in the micro-CT images designated as the bone, and BV/TV is the ratio of the bone volume to the total area of interest. In this case, Tb.Th is designated as the mean thickness of the trabecular bone. As seen in the micro-CT images, there was minimal cartilage and bone growth in the Li0 group at 8 and 12 weeks after implantation. From the 12-week-old Li0 group, it could be seen that there was a huge defect, which could have been due to cyst formation or minimal bone formation. It has been verified that the pore size ranging from 200 to 500 μ m was suitable for bone tissue regeneration [44]. In contrast, in the Li10 group, increased bone growth was observed, as evidenced by the increased trabeculae and osteophyte formation. The majority of the trabecular region was filled with fatty tissue and bone marrow, with only 20% filled with bone. This allowed for the absorption and transfer of compressive stress from articular surfaces to the cortical bones. Furthermore, there was an increase in cartilaginous tissue growth and invasion in the trabecular region of Li10. This was expected, as the subchondral and underlying trabecular regions supposedly comprise articular cartilage and subchondral bone. In the Li10 group, multiple vascular invasions and channels were observed in the trabecular region. Statistically, there was a time-dependent effect for both BV/TV and Tb.Th ratios, with significant increases in BV/TV and Tb.Th for the Li10 group compared with the Li0 group at all time points. In addition, Li10 had significantly higher BV/TV ratios than Li5 at 8 and 12 weeks and significantly higher Tb.Th ratios than Li5 after 12 weeks of implantation. Specifically, Li10 had $1.9 \times$ and $1.3 \times$ higher BV/TV ratios at 12 weeks than Li0 and Li5, respectively. Taken together, it can be concluded that adding Li to CS scaffolds upregulated the chondrogenic and osteogenic capabilities of CS scaffolds.

The harvested samples at 8 and 12 weeks after implantation were further histologically examined by HE, AB, MT, and VK staining, as shown in Fig. 6D. As seen from the HE results for Li10, after 8 weeks of implantation, there was a clear tidemark between the regenerated cartilage and its underlying subchondral bone. However, there were no clear tidemark borders for Li0 at 12 weeks after implantation. Minimal and sparse cartilage tissue was observed on the articular surface in the Li0 group at week 8. This was further supported by the AB staining results, whereby intense AB staining was observed in the Li10 groups after 8 weeks of implantation. For Li0 and Li5, the cartilage tissues on the articular surfaces were inconsistent and irregular at week 8. Four weeks after implantation, the articular surface of Li0 was still not fully covered with a layer of cartilage, and a huge cartilaginous defect was noted in the middle of the articular region. For bone regeneration, there were increased interconnected trabecular networks with osteoblast or osteocyte lacunae among the networks. At week 8, bone tissues were observed to have invaded and grown into the scaffolds of Li10, whereas the scaffolds of Li0 were still generally intact (Fig. 6E). At week 12, the residual scaffolds were embedded among the regenerated bone tissues, implying that our scaffolds had stable degradation rates and could support regeneration up to 12 weeks after implantation. These results were supported by MT staining, whereby Li10 showed more intense blue staining than Li5 and Li0 at both time points, which indicated higher levels of bone and cartilage regeneration in the Li10 group. VK staining was performed to determine the mineralization levels. The VK results clearly showed that Li10 had the highest levels of mineralization compared with those of the other groups. These results confirmed that our LiCS scaffolds enhanced the chondrogenic and osteogenic capabilities of the CS scaffolds. Based on the staining results above, it can be

preliminarily suggested that CS scaffolds alone cannot fully support cartilage and bone regeneration and that further modifications, such as the addition of Li, are required to enhance the capabilities of CS scaffolds.

3.6. Effect of LiCS scaffolds stimulates WJMSC-derived exosomes to regulate osteochondral regeneration

Our previous data showed that LiCS scaffolds can promote bone regeneration and repair cartilage defects. Although various studies have speculated on the possible mechanism, there are still uncertainties [45, 46]. Therefore, this study analyzed the effect of LiCS scaffolds from the perspective of exosomes. In recent years, exosomes have become a trending research topic in regenerative medicine because of their high regenerative potency and versatile applicability [47,48]. Exosomes deliver functional molecules, such as bioactive lipids, proteins, cytokines, and RNA species, from MSCs to recipient cells and participate in intercellular communication and tissue regeneration [49]. Therefore, we intended to explore whether LiCS scaffolds could influence the content and quantity of exosomes secreted by WJMSCs, and the results are shown in Fig. 7. First, we analyzed exosome-related biomarkers including CD63, CD9, Alix, HSP70, and TSG101 by western blotting, and the results are shown in Fig. 7A. The Li10 group showed the highest expression of every exosome marker among all groups, whereas the Li5 group showed markedly increased expression of all exosome surface markers compared with the Li0 group. The TEM images revealed that the secreted exosomes from all groups were approximately 150 nm in diameter and round (Fig. 7B). Furthermore, NTA showed a similar size distribution within 120–150 nm in all groups (Fig. 7C). As a result, the presence of exosomes was confirmed by size determination because of the size of exosomes reported to be 50–200 nm, different from micro-vesicles and apoptotic bodies [50]. However, the precise roles of these markers in osteogenesis and chondrogenesis remain unclear. Fig. 7D shows that the total amount of protein per exosome was significantly higher in the Li10 group than that in the Li5 and Li0 groups ($p < 0.05$). Lastly, we labeled different exosomes stimulated by LiCS with a fluorescent dye to evaluate the uptake of exosomes by WJMSCs (Fig. 7E) and found that the number of exosomes taken up by WJMSCs was remarkably greater than in the Li5 and Li10 group. Based on the above results, we observed that the LiCS scaffolds enabled WJMSCs to secrete exosomes with more intra- and extracellular proteins, thus increasing the number of exosomes. In addition, exosomes from Li10-treated medium were more easily taken up by WJMSCs. These features provide LiCS scaffolds with potential applications in the field of regenerative medicine. However, further studies are required to confirm the effects of the secreted exosomes.

In order to investigate how LiCS scaffolds regulated inflammation, angiogenesis, osteogenesis, and chondrogenesis, we performed transcriptome analysis to examine the miRNA expression between Li0 and Li10, and further detailed GO and KEGG analysis selected Li10 significant difference to Li0 from the compared data. The results of the heatmap as shown in Fig. 7F and volcano map in Fig. 7G analyses revealed that 3150 DEGs were upregulated in the Li10 group, whereas 1426 miRNAs were downregulated. We surveyed the vital mediators of miRNAs involved in cartilage regeneration, angiogenesis, and anti-inflammation and screened out five potential miRNAs for bone regeneration according to the log value and read counts as follows: miR-210-3p, miR-324-3p, miR-496, miRNA-218, and miRNA-126. Angiogenic miRNA, found in Li10 exosome included miRNA-125, miR-210-3p, miRNA-126, miR-942-5p, and miRNA-26. Finally, the anti-inflammatory activities of miRNA-125, miR-320d, miR-193b-3p, miR-210-3p, and miR-18a-5p were evaluated. In the miRNA DEG results, miR-210-3p was predicted to be highly correlated with the three miRNAs functionally expressed in cells, followed by miR-125, which has a high potential to regulate angiogenesis and anti-inflammation. In previous studies, miR-210-3p was found to work through the EFNA3/PI3K/

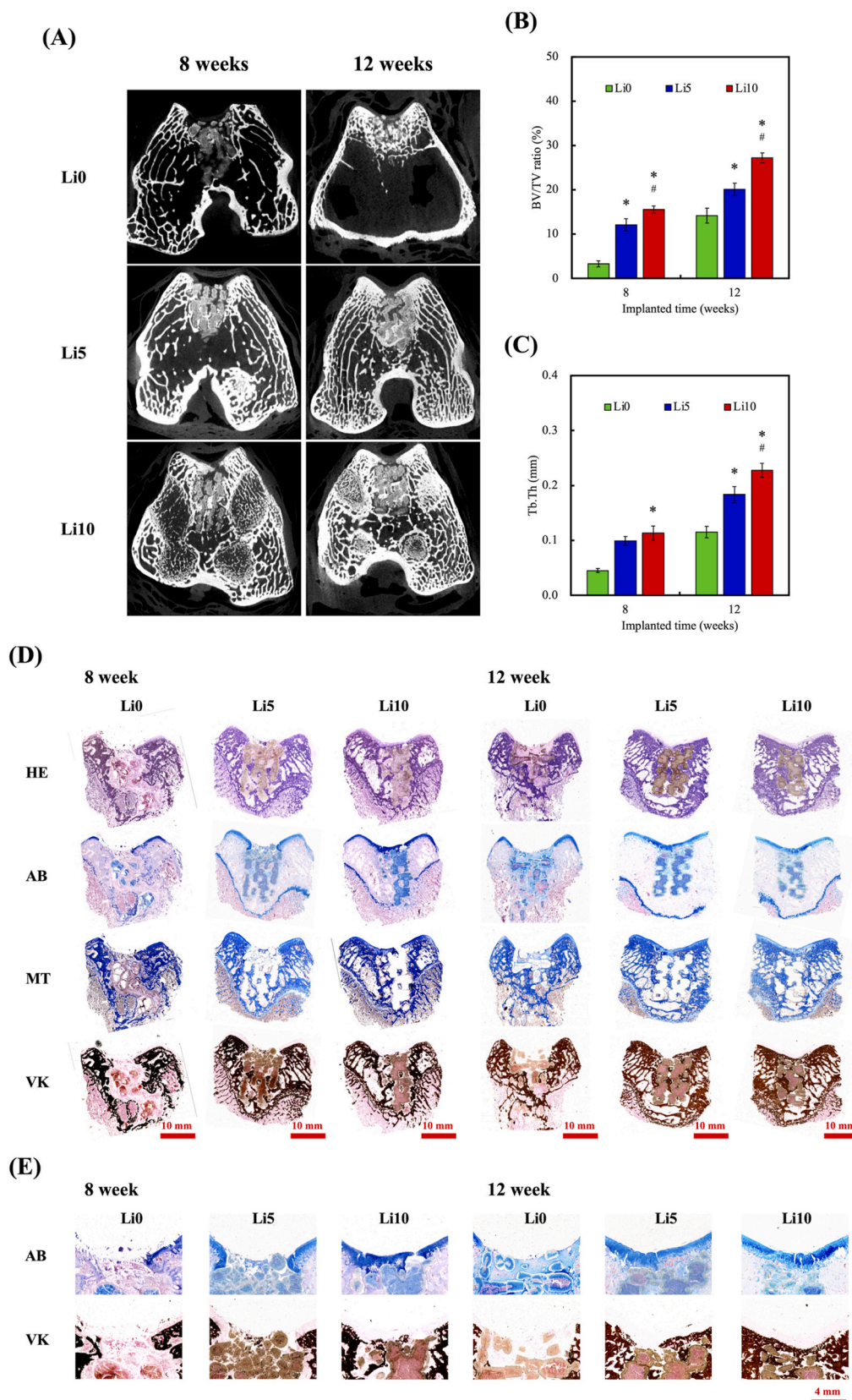


Fig. 6. The evaluation of the implanted scaffolds using micro-CT imaging, quantitative analysis of bone volume and trabecular thickness, and histological staining techniques to assess the cellular response, extracellular matrix composition, and mineralization over different time implantation. (A) Micro-CT images; (B) BV/TV ratio and (C) Tb.Th after 8- and 12-week implantations of Li0, Li5, and Li10 scaffolds. (D) Histological staining: hematoxylin and eosin (HE), Alcian blue (AB), Masson's trichrome (MT), and Von Kossa (VK) staining of Li0, Li5, and Li10 after 8 and 12 weeks of implantation.

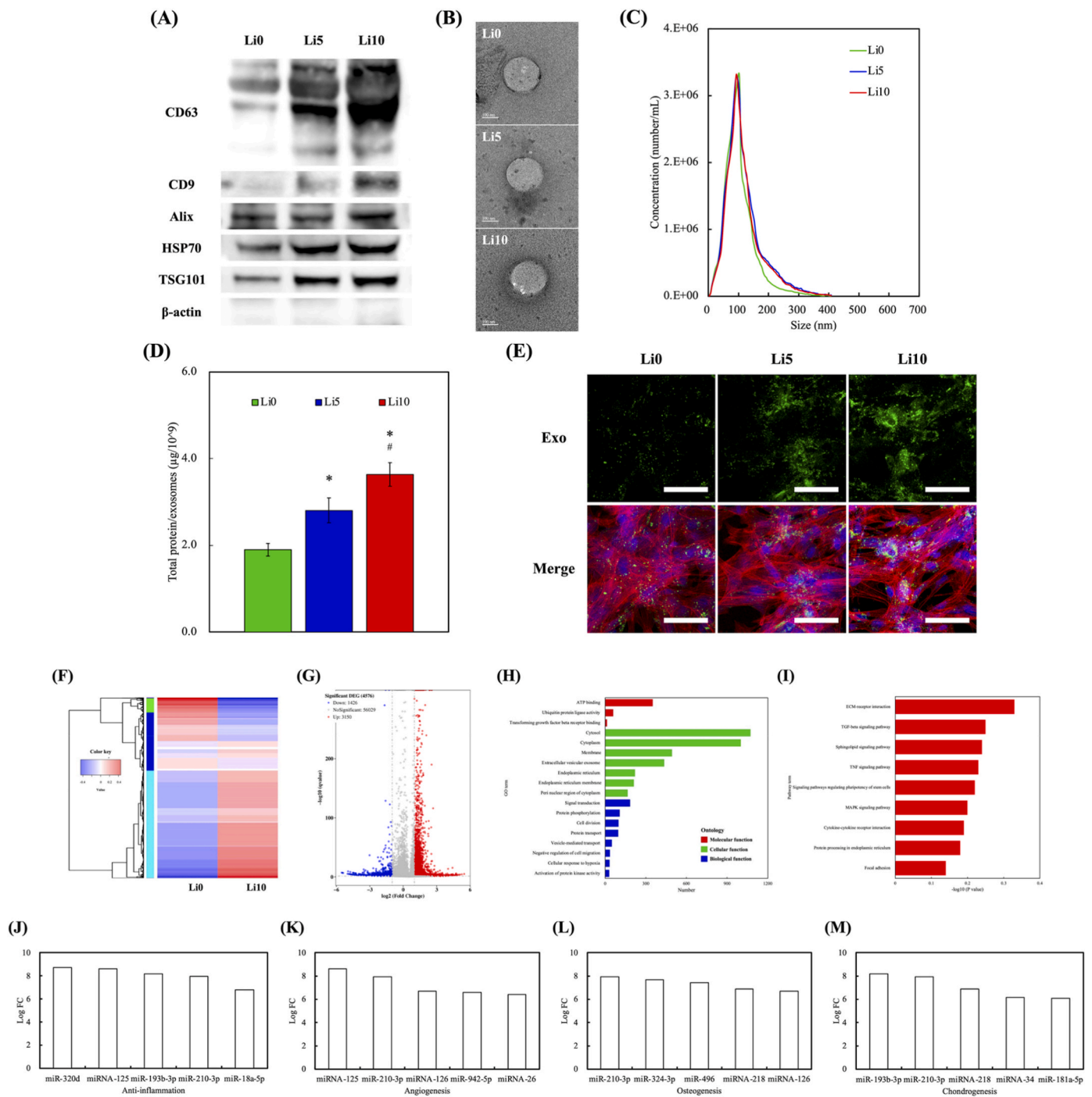


Fig. 7. The characterization and analysis of WJMSC-derived exosomes stimulated by LiCS. (A) Western blot of exosome markers CD63, CD9, Alix, HSP70, and TSG101; (B) transmission electron microscopy (TEM) image of exosome; (C) concentrations and size of exosomes; (D) total proteins per exosomes; and (E) fluorescence microscopy of exosomes. (F) Hierarchical clustering heatmap and (G) differential expression of genes between Li10 and Li0 groups. The up-regulated, down-regulated, and unchanged genes were dotted in red, green, and gray, respectively. (H) GO enrichment of up-regulated miRNAs. (I) Significant terms of different functions in the top nine up-regulated pathways of KEGG pathway. The transcriptome data was performed to determine the expression of miRNAs in (J) anti-inflammation processes, (K) angiogenesis, (L) osteogenesis, and (M) chondrogenesis.

AKT pathway by utilizing hypo-sEVs and can be useful for enhancing vascularized bone regeneration [51]. Other studies have indicated that miR-210-3p enhances osteogenic gene expression *in vitro* and promotes subcutaneous critical-size load-bearing bone defects in a mouse model of bone regeneration using miR-210-3p/ β -tricalcium phosphate (β -TCP) with bone marrow stem cells [52]. In recent studies on miR-210-3p, hUCMSC-derived exosomes were found to improve cardiac function by targeting EFNA3 to improve the angiogenesis of miR-210-3p, promote

angiogenesis around the heart, promote proliferation, inhibit cell apoptosis, and reduce fibrosis [50]. These results demonstrate that Li10-stimulated exosomes have high application value for tissue regeneration. Furthermore, the GO terms enriched in Li10 up-regulated genes were significantly correlated with actin cytosol, cytoplasm, protein phosphorylation, cell membrane, endoplasmic reticulum membrane, and bone regeneration processes (Fig. 7H). To further investigate the possible mechanisms underlying the effects of miRNAs on osteoblast

function, the upregulated miRNAs were subjected to GO and KEGG analyses to identify the pathways controlled by Li10. Notably, KEGG predicted Li10-stimulated exosomes were closely associated with the ECM-receptor interaction, MAPK signaling pathway, cytokine–cytokine receptor interaction, and TGF- β signaling pathway (Fig. 7I). Among the pathways upregulated in Li10, the MAPK signaling pathway, previously proven to be associated with osteocyte dedifferentiation, was enriched. Hao et al. showed that the MAPK member p38 signaling pathway was activated, and the s10ZS/HA/Col scaffolds regulated the behavior of monocytes and facilitated the formation of a favorable microenvironment that promoted the migration and differentiation of BMSCs and induced angiogenesis [53]. Su et al. demonstrated that a PPEA biomimetic periosteum with Schwann cell exosomes has multi-cell functional regulators, such as neurogenic, angiogenic, and osteogenic effects, through the JNK3 MAPK pathway. Moreover, the ECM receptor inactivation signaling pathway was enriched in the Li10-stimulated exosomes. This pathway is associated with the regulation of multiple biological processes such as cell differentiation, proliferation, migration, and apoptosis. These signaling pathways are essential for bone formation and remodeling, and their activation can stimulate osteoblast differentiation and extracellular matrix formation [54,55]. Furthermore, the cytokine–cytokine receptor interactions in Li10-stimulated exosomes suggest that the exosomes can modulate the inflammatory response (Fig. 7J), in particular the production of inflammatory cytokines, including TNF- α , IL-1 β , and IL-6. These findings indicate that Li10-stimulated exosomes may mediate multiple pathways to promote angiogenesis (Fig. 7K) and osteogenesis (Fig. 7L). The anti-inflammation miRNA was found via transcriptome analysis have excellent suppress pro-inflammatory expression from previous literature [56]. This evidence makes us more confident that the Li10 composite scaffold has these good benefits to help the surrounding injured bone tissue to promote regeneration. In addition, chondrogenic differentiation of WJMSCs was regulated by exosomal miR-210 to affect β -catenin pathways that contain various growth factors, such as TGF- β 1, BMPs, and IGF-1 [57].

Several studies have identified the potential to regulate chondrogenesis through miRNA expression [58]. We present the top five miRNAs that have been identified as potential regulators of chondrogenesis based on their expression levels and functional roles: miR-193b-3p, miR-210-3p, miRNA-218, miRNA-34 and miR-181a-5p (Fig. 7M). These miRNAs have been shown to play important roles in various aspects of chondrogenesis, including the proliferation and differentiation of chondrocytes, extracellular matrix synthesis, and cartilage homeostasis. In miRNA DEGs results, it was found that miR-210-3p is consistently expressed in bone regeneration, angiogenesis, anti-inflammation, and chondrogenesis. These findings suggest that miR-210-3p may play a critical role in regulating multiple cellular behaviors involved in tissue regeneration and repair. Followed by miR-125 having a high potential to regulate anti-inflammation, angiogenesis and chondrogenesis. Our results found miR-125 high potential regulation of functional behaviors for cartilage regeneration, chondrocyte neo vessel formation that may have significant implications for the treatment of cartilage injuries and bone defect diseases, such as osteoarthritis, which are characterized by a loss of cartilage tissue. These results displayed of Li10 group had high application value for tissue regeneration. Both miR-210 and miR-125 have emerged as promising regulators of bone and cartilage regeneration, respectively. Studies have shown that miR-210 plays a key role in osteogenic differentiation signaling pathway, promoting mineralization and regulating bone remodeling through its effects on osteoblasts and osteoclasts. Similarly, miR-125 has been found to modulate chondrogenic differentiation and cartilage homeostasis by regulating the expression of key genes involved in extracellular matrix synthesis and chondrocyte proliferation. The results indicated MAPK pathway was predicted consists of a complex network of intracellular signaling cascades that can be activated by various extracellular stimuli, including growth factors and cytokines [59]. Moreover, recent studies have suggested that these miRNAs could be harnessed for dual-purpose

regeneration strategies by encapsulating them in extracellular vesicles. By packaging miR-210 and miR-125 into vesicles, they can be delivered to bone and cartilage tissue with high specificity, leading to enhanced repair of both hard and soft tissue defects. This approach has shown promising results in animal models, with vesicle-encapsulated miR-210 and miR-125 leading to improved bone and cartilage repair compared to unencapsulated miRNAs or control treatments. Overall, the ability of miR-210 and miR-125 to regulate bone and cartilage regeneration, respectively, and their potential for dual-purpose regenerative applications make them attractive candidates for further investigation and development as therapeutic agents in regenerative medicine [48]. In summary, our results demonstrate that Li10 group stimulation plays a crucial role in promoting anti-inflammatory responses, chondrogenesis, and proliferation, as well as neo vessel formation during the early stages of osteocyte differentiation. These effects ultimately contribute to enhanced cell mineralization and cartilage regeneration. These findings provide important insights into the mechanisms underlying the bone-cartilage dual-healing efficacy of Li10 group. Overall, our findings suggest that LiCS-stimulated exosomes modulate the osteogenic process and promote osteochondral healing. Our study provides an insight into the potential of exosomes as a therapeutic approach for osteochondral regeneration.

4. Conclusion

In this study, we successfully modified the surfaces of CS scaffolds with Li ions using a simple immersion technique. Individually, both CS and Li have been proven to be potent candidates for bone and cartilage regeneration. However, to date, there have been no reports on the combination of both elements for osteochondral regeneration. Our results showed that Li could be coated onto the surfaces of the CS scaffolds via a simple immersion technique without affecting the structural integrity of CS scaffolds. Hydrophilicity and surface roughness were found to be significantly enhanced by Li modification in a dose-dependent manner, which could have contributed to enhanced cellular adhesion, viability, and proliferation, as seen in immunofluorescence studies. Li modification also improved the degradation rates and residual mechanical properties of the scaffolds, making them better candidates for clinical applications. As hypothesized, Li was found to improve cartilage regeneration, as shown by the upregulation of cartilage-related markers such as Col II and GAG. Notably, osteogenic-related markers such as ALP, BSP, OC, and related histological staining were also enhanced with increasing Li modifications. Subsequent *in vivo* studies proved that our scaffolds were indeed able to support osteochondral regeneration better than traditional CS scaffolds. Further investigations confirmed significant differences in the levels of exosomes secreted via stimulation by LiCS scaffolds, implying that exosomes play a role in Li-related osteochondral regeneration. Taken together, our studies showed that LiCS scaffolds could be easily modified for tissue engineering and that further evaluations are required to understand the mechanism behind these surface modifications.

Credit author statement

Tsung-Li Lin: Writing – original draft preparation; **Yen-Hong Lin:** Conceptualization, Writing – original draft preparation; **Alvin Kai-Xing Lee:** Methodology, Investigation; **Ting-You Kuo, Cheng-Yu Chen, Kun-Hao Chen, and Yun-Ting Chou:** Investigation and Data curation; **Yi-Wen Chen:** Funding acquisition, Writing-Reviewing, and Editing; **Ming-You Shie:** Supervision, Validation, Visualization, Writing-Reviewing, and Editing.

Declaration of competing interest

The authors declare that they have no known competing financial interests or personal relationships that could have appeared to influence

the work reported in this paper.

Data availability

No data was used for the research described in the article.

Acknowledgements

The authors acknowledge receipt of a grant from the National Science and Technology Council (NSTC 111-2314-B-039-050-MY2 and 111-2314-B-039-082) of Taiwan, and China Medical University Hospital grants (DMR-111-058) of Taiwan. Experiments and data analysis were performed in part through the use of the Medical Research Core Facilities, Office of Research & Development at China Medical University, Taichung, Taiwan. The authors declare that they have no conflicts of interest.

References

- [1] C. Lesage, M. Lafont, P. Guihard, P. Weiss, J. Guicheux, V. Delplace, Material-assisted strategies for osteochondral defect repair, *Adv. Sci.* 9 (2022), 2200050.
- [2] M. Nelson, S. Li, S.J. Page, X. Shi, P.D. Lee, M.M. Stevens, J.V. Hanna, J.R. Jones, 3D printed silica-gelatin hybrid scaffolds of specific channel sizes promote collagen Type II, Sox9 and Aggrecan production from chondrocytes, *Mater. Sci. Eng. C* 123 (2021), 111964.
- [3] T.J. Ji, B. Feng, J. Shen, M. Zhang, Y.Q. Hu, A.X. Jiang, D.Q. Zhu, Y.W. Chen, W. Ji, Z. Zhang, H. Zhang, F. Li, An avascular niche created by axitinib-loaded PCL/collagen nanofibrous membrane stabilized subcutaneous chondrogenesis of mesenchymal stromal cells, *Adv. Sci.* 8 (2021), 2100351.
- [4] Y. Hua, Y. Huo, B. Bai, J. Hao, G. Hu, Z. Ci, X. Wu, M. Yu, X. Wang, H. Chen, W. Ren, Y. Zhang, X. Wang, G. Zhou, Fabrication of biphasic cartilage-bone integrated scaffolds based on tissue-specific photo-crosslinkable acellular matrix hydrogels, *Mater Today Bio* 17 (2022), 100489.
- [5] C. Shu, C. Qin, L. Chen, Y. Wang, Z. Shi, J. Yu, J. Huang, C. Zhao, Z. Huan, C. Wu, M. Zhu, Y. Zhu, Metal-organic framework functionalized bioceramic scaffolds with antioxidative activity for enhanced osteochondral regeneration, *Adv. Sci.* 10 (2023), 2206875.
- [6] C.T. Kao, C.C. Lin, Y.W. Chen, C.H. Yeh, H.Y. Fang, M.Y. Shie, Poly(dopamine) coating of 3D printed poly(lactic acid) scaffolds for bone tissue engineering, *Mater Sci Eng C Mater Biol Appl* 56 (2015) 165–173.
- [7] C.C. Ho, Y.W. Chen, K. Wang, Y.H. Lin, T.C. Chen, M.Y. Shie, Effect of mussel-inspired polydopamine on the reinforced properties of 3D printed β -tricalcium phosphate/polycaprolactone scaffolds for bone regeneration, *J. Mater. Chem. B* 11 (2023) 72–82.
- [8] Y.H. Lin, K.X. Lee, C.C. Ho, M.J. Fang, T.Y. Kuo, M.Y. Shie, The effects of a 3D-printed magnesium-/strontium-doped calcium silicate scaffold on regulation of bone regeneration via dual-stimulation of the AKT and WNT signaling pathways, *Biomater Adv* 135 (2022), 112660.
- [9] J.J. Lee, H.Y. Ng, Y.H. Lin, E.W. Liu, T.J. Lin, H.T. Chiu, X.R. Ho, H.A. Yang, M. Y. Shie, The 3D printed conductive grooved topography hydrogel combined with electrical stimulation for synergistically enhancing wound healing of dermal fibroblast cells, *Biomater Adv* 142 (2022), 213132.
- [10] Y.W. Chen, K. Wang, C.C. Ho, C.T. Kao, H.Y. Ng, M.Y. Shie, Cyclic tensile stimulation enrichment of Schwann cell-laden auxetic hydrogel scaffolds towards peripheral nerve tissue engineering, *Mater. Des.* 195 (2020), 108982.
- [11] Y.W. Chen, Y.F. Shen, C.C. Ho, J. Yu, Y.H.A. Wu, K. Wang, C.T. Shih, M.Y. Shie, Osteogenic and angiogenic potentials of the cell-laden hydrogel/mussel-inspired calcium silicate complex hierarchical porous scaffold fabricated by 3D bioprinting, *Mater. Sci. Eng. C* 91 (2018) 679–687.
- [12] L. Chen, C. Deng, J. Li, Q. Yao, J. Chang, L. Wang, C. Wu, 3D printing of a lithium-calcium-silicate crystal bioscaffold with dual bioactivities for osteochondral interface reconstruction, *Biomaterials* 196 (2019) 138–150.
- [13] V. Bunpetch, X. Zhang, T. Li, J. Lin, E.P. Maswikiti, Y. Wu, D. Cai, J. Li, S. Zhang, C. Wu, H. Ouyang, Silicate-based bioceramic scaffolds for dual-lineage regeneration of osteochondral defect, *Biomaterials* 192 (2019) 323–333.
- [14] M. Wu, F. Chen, H. Liu, P. Wu, Z. Yang, Z. Zhang, J. Su, L. Cai, Y. Zhang, Bioinspired sandwich-like hybrid surface functionalized scaffold capable of regulating osteogenesis, angiogenesis, and osteoclastogenesis for robust bone regeneration, *Mater Today Bio* 17 (2022), 100458.
- [15] M.Y. Shie, S.J. Ding, H.C. Chang, The role of silicon in osteoblast-like cell proliferation and apoptosis, *Acta Biomater.* 7 (2011) 2604–2614.
- [16] N. Salam, I.R. Gibson, Lithium ion doped carbonated hydroxyapatite compositions: synthesis, physicochemical characterisation and effect on osteogenic response in vitro, *Biomater Adv* 140 (2022), 213068.
- [17] C. Pan, L. Chen, R. Wu, H. Shan, Z. Zhou, Y. Lin, X. Yu, L. Yan, C. Wu, Lithium-containing biomaterials inhibit osteoclastogenesis of macrophages in vitro and osteolysis in vivo, *J. Mater. Chem. B* 6 (2018) 8115–8126.
- [18] Z. Wu, J. Bai, G. Ge, T. Wang, S. Feng, Q. Ma, X. Liang, W. Li, W. Zhang, Y. Xu, K. Guo, W. Cui, G. Zha, D. Geng, Regulating macrophage polarization in high glucose microenvironment using lithium-modified bioglass-hydrogel for diabetic bone regeneration, *Adv Healthc Mater* 11 (2022), 2200298.
- [19] F. He, X. Yuan, T. Lu, Y. Wang, S. Feng, X. Shi, L. Wang, J. Ye, H. Yang, Preparation and characterization of novel lithium magnesium phosphate bioceramic scaffolds facilitating bone generation, *J. Mater. Chem. B* 10 (2022) 4040–4047.
- [20] Z. Tang, Y. Lu, S. Zhang, J. Wang, Q. Wang, Y. Xiao, X. Zhang, Chondrocyte secretome enriched microparticles encapsulated with the chondrocyte membrane to facilitate the chondrogenesis of BMSCs and reduce hypertrophy, *J. Mater. Chem. B* 9 (2021) 9989–10002.
- [21] X. Wang, B. Guo, Q. Li, J. Peng, Z. Yang, A. Wang, D. Li, Z. Hou, K. Lv, G. Kan, H. Cao, H. Wu, J. Song, X. Pan, Q. Sun, S. Ling, Y. Li, M. Zhu, P. Zhang, S. Peng, X. Xie, T. Tang, A. Hong, Z. Bian, Y. Bai, A. Lu, Y. Li, F. He, G. Zhang, Y. Li, miR-214 targets ATF4 to inhibit bone formation, *Nat. Med.* 19 (2013) 93–100.
- [22] Q. Li, Y. Deng, X. Liu, Delivering multifunctional peptide-conjugated gene carrier/miRNA-218 complexes from monodisperse microspheres for bone regeneration, *ACS Appl. Mater. Interfaces* 14 (2022) 42904–42914.
- [23] H.P. Bei, P.M. Hung, H.L. Yeung, S. Wang, X. Zhao, Bone-a-petite: engineering exosomes towards bone, osteochondral, and cartilage repair, *Small* 17 (2021), 2101741.
- [24] K.Y. Chen, C.H. Yao, Repair of bone defects with gelatin-based composites: a review, *Biomedicine* 1 (2011) 29–32.
- [25] Y. Wang, C. Ling, J. Chen, H. Liu, Q. Mo, W. Zhang, Q. Yao, 3D-printed composite scaffold with gradient structure and programmed biomolecule delivery to guide stem cell behavior for osteochondral regeneration, *Biomater Adv* 140 (2022), 213067.
- [26] F.C. Oliveira, J.O. Carvalho, L.S.S.M. Magalhães, J.M. da Silva, S.R. Pereira, A.L. G. Júnior, L.M. Soares, L.I.C. Cariman, R.I. da Silva, B.C. Viana, E.C. Silva-Filho, S. Afewerki, H.N. da Cunha, M.L. Vega, F.R. Marciano, A.O. Lobo, Biomimetic mineralization inspired engineering of nanobiomaterials promoting bone repair, *Mater. Sci. Eng. C* 120 (2021), 111776.
- [27] J. Li, Q. Yao, Y. Xu, H. Zhang, L.L. Li, L. Wang, Lithium chloride-releasing 3D printed scaffold for enhanced cartilage regeneration, *Med Sci Monit* 25 (2019) 4041–4050.
- [28] F. Zhang, M. Zhou, W. Gu, Z. Shen, X. Ma, F. Lu, X. Yang, Y. Zheng, Z. Gou, Zinc-/copper-substituted dicalcium silicate cement: advanced biomaterials with enhanced osteogenesis and long-term antibacterial properties, *J. Mater. Chem. B* 8 (2020) 1060–1070.
- [29] X. Wang, J. Fang, W. Zhu, C. Zhong, D. Ye, M. Zhu, X. Lu, Y. Zhao, F. Ren, Bioinspired highly anisotropic, ultrastrong and stiff, and osteoconductive mineralized wood hydrogel composites for bone repair, *Adv. Funct. Mater.* 31 (2021), 2010068.
- [30] S.A. Naghavi, C. Sun, M. Hejazi, M. Tamaddon, J. Zheng, L. Wang, C. Zhang, S. N. Varma, D. Li, M. Moazen, L. Wang, C. Liu, On the mechanical aspect of additive manufactured polyether-ether-ketone scaffold for repair of large bone defects, *Biomater. Transl* 3 (2022) 142–151.
- [31] E. Saygili, P. Saglam-Metiner, B. Cakmak, E. Alarcin, G. Beceren, P. Tulum, Y.-W. Kim, K. Gunes, G.G. Eren-Ozcan, D. Akakin, J.-Y. Sun, O. Yesil-Celiktas, Bilayered laponite/alginate-poly(acrylamide) composite hydrogel for osteochondral injuries enhances macrophage polarization: an in vivo study, *Biomater Adv* 134 (2022), 112721.
- [32] Y. Chen, H.C. Whetstone, A.C. Lin, P. Nadesan, Q. Wei, R. Poon, B.A. Alman, Beta-catenin signaling plays a disparate role in different phases of fracture repair: implications for therapy to improve bone healing, *PLoS Med.* 4 (2007) e249.
- [33] A. Zareidoost, M. Yousefpour, B. Ghaseme, A. Amanzadeh, The relationship of surface roughness and cell response of chemical surface modification of titanium, *J. Mater. Sci. Mater. Med.* 23 (2012) 1479–1488.
- [34] P. Keikhosravi, H. Maleki-Ghaleh, A.K. Khosrowshahi, M. Bodaghi, Z. Dargahi, M. Kavanlouei, P. Khademi-Azandehi, A. Fallah, Y. Beygi-Khosrowshahi, M. H. Siadat, Bioactivity and antibacterial behaviors of nanostructured lithium-doped hydroxyapatite for bone scaffold application, *Int. J. Mol. Sci.* 22 (2021) 9214.
- [35] W.C. Liu, C.C. Hu, Y.Y. Tseng, R. Sakthivel, K.S. Fan, A.N. Wang, Y.M. Wang, R. J. Chung, Study on strontium doped tricalcium silicate synthesized through sol-gel process, *Mater. Sci. Eng. C* 108 (2020), 110431.
- [36] L. Liu, F. Yu, L. Chen, L. Xia, C. Wu, B. Fang, Lithium-containing biomaterials stimulate cartilage repair through bone marrow stromal cells-derived exosomal miR-455-3p and histone H3 acetylation, *Adv Healthc Mater* 12 (2023), 2202390.
- [37] C. Deng, J. Chang, C. Wu, Bioactive scaffolds for osteochondral regeneration, *J Orthop Translat* 17 (2019) 15–25.
- [38] L. Li, X. Peng, Y. Qin, R. Wang, J. Tang, X. Cui, T. Wang, W. Liu, H. Pan, B. Li, Acceleration of bone regeneration by activating Wnt/ β -catenin signalling pathway via lithium released from lithium chloride/calcium phosphate cement in osteoporosis, *Sci Rep-Uk* 7 (2017), 45204.
- [39] W. Noble, E. Planel, C. Zehr, V. Olm, J. Meyerson, F. Suleman, K. Gaynor, L. Wang, J. LaFrancois, B. Feinstein, M. Burns, P. Krishnamurthy, Y. Wen, R. Bhat, J. Lewis, D. Dickson, K. Duff, Inhibition of glycogen synthase kinase-3 by lithium correlates with reduced tauopathy and degeneration in vivo, *Proc. Natl. Acad. Sci. USA* 102 (2005) 6990–6995.
- [40] C. Haxaire, E. Hayj, V. Geoffroy, Runx2 controls bone resorption through the down-regulation of the Wnt pathway in osteoblasts, *Am. J. Pathol.* 186 (2016) 1598–1609.
- [41] P. Han, M. Xu, J. Chang, N. Chakravorty, C. Wu, Y. Xiao, Lithium release from β -tricalcium phosphate inducing cementogenic and osteogenic differentiation of both hPDLcs and hBMSCs, *Biomater Sci-Uk* 2 (2014) 1230–1243.
- [42] Y. Yuan, Q. Yuan, C. Wu, Z. Ding, X. Wang, G. Li, Z. Gu, L. Li, H. Xie, Enhanced osteoconductivity and osseointegration in calcium polyphosphate bioceramic

- scaffold via lithium doping for bone regeneration, *ACS Biomater. Sci. Eng.* 5 (2019) 5872–5880.
- [43] T. Minashima, Y. Zhang, Y. Lee, T. Kirsch, Lithium protects against cartilage degradation in osteoarthritis, *Arthritis Rheumatol.* 66 (2014) 1228–1236.
- [44] N. Tien, J.J. Lee, K.X. Lee, Y.H. Lin, J.X. Chen, T.Y. Kuo, M.Y. Shie, Additive manufacturing of caffeic acid-inspired Mineral Trioxide Aggregate/poly-ε-caprolactone scaffold for regulating vascular induction and osteogenic regeneration of dental pulp stem cells, *Cells* 10 (2021) 2911.
- [45] C. Deng, Q. Yang, X. Sun, L. Chen, C. Feng, J. Chang, C. Wu, Bioactive scaffolds with Li and Si ions-synergistic effects for osteochondral defects regeneration, *Appl. Mater. Today* 10 (2018) 203–216.
- [46] Y. Hu, L. Chen, Y. Gao, P. Cheng, L. Yang, C. Wu, Q. Jie, A lithium-containing biomaterial promotes chondrogenic differentiation of induced pluripotent stem cells with reducing hypertrophy, *Stem Cell Res. Ther.* 11 (2020), 77–13.
- [47] Y.S. Chen, H.Y. Ng, Y.W. Chen, D.Y. Cho, C.C. Ho, C.Y. Chen, S.C. Chiu, Y.R. Jhong, M.Y. Shie, Additive manufacturing of Schwann cell-laden collagen/alginate nerve guidance conduits by freeform reversible embedding regulate neurogenesis via exosomes secretion towards peripheral nerve regeneration, *Biomater Adv* 146 (2023), 213276.
- [48] Z. Yan, H. Yin, J. Wu, G. Tian, M. Li, Z. Liao, S. He, H. Deng, C. Ning, Z. Ding, X. Yuan, X. Sui, M. Chen, S. Liu, Q. Guo, Engineering exosomes by three-dimensional porous scaffold culture of human umbilical cord mesenchymal stem cells promote osteochondral repair, *Mater Today Bio* 19 (2023), 100549.
- [49] W. Yu, S. Li, X. Guan, N. Zhang, X. Xie, K. Zhang, Y. Bai, Higher yield and enhanced therapeutic effects of exosomes derived from MSCs in hydrogel-assisted 3D culture system for bone regeneration, *Biomater Adv* 133 (2022), 112646.
- [50] A.N.V.L. Kavya, S. Subramanian, S. Ramakrishna, Therapeutic applications of exosomes in various diseases: a review, *Biomaterials Adv* 134 (2022), 112579.
- [51] Y. Zhuang, M. Cheng, M. Li, J. Cui, J. Huang, C. Zhang, J. Si, K. Lin, H. Yu, Small extracellular vesicles derived from hypoxic mesenchymal stem cells promote vascularized bone regeneration through the miR-210-3p/EFNA3/PI3K pathway, *Acta Biomater.* 150 (2022) 413–426.
- [52] B. Hu, Y. Li, M. Wang, Y. Zhu, Y. Zhou, B. Sui, Y. Tan, Y. Ning, J. Wang, J. He, C. Yang, D. Zou, Functional reconstruction of critical-sized load-bearing bone defects using a Sclerostin-targeting miR-210-3p-based construct to enhance osteogenic activity, *Acta Biomater.* 76 (2018) 275–282.
- [53] Y. Song, H. Wu, Y. Gao, J. Li, K. Lin, B. Liu, X. Lei, P. Cheng, S. Zhang, Y. Wang, J. Sun, L. Bi, G. Pei, Zinc silicate/nano-hydroxyapatite/collagen scaffolds promote angiogenesis and bone regeneration via the p38 MAPK pathway in activated monocytes, *ACS Appl. Mater. Interfaces* 12 (2020) 16058–16075.
- [54] R.K. Singh, D.S. Yoon, N. Mandakhbayar, C. Li, A.G. Kurian, N.H. Lee, J.H. Lee, H. W. Kim, Diabetic bone regeneration with nanoceria-tailored scaffolds by recapitulating cellular microenvironment: activating integrin/TGF-β co-signaling of MSCs while relieving oxidative stress, *Biomaterials* 288 (2022), 121732.
- [55] M. Deng, J. Tan, C. Hu, T. Hou, W. Peng, J. Liu, B. Yu, Q. Dai, J. Zhou, Y. Yang, R. Dong, C. Ruan, S. Dong, J. Xu, Modification of PLGA scaffold by MSC-derived extracellular matrix combats macrophage inflammation to initiate bone regeneration via TGF-β-induced protein, *Adv Healthc Mater* 9 (2020), 2000353.
- [56] C. Huang, W. Zhong, X. Ren, X. Huang, Z. Li, C. Chen, B. Jiang, Z. Chen, X. Jian, L. Yang, X. Liu, H. Huang, C. Shen, X. Chen, X. Dou, B. Yu, MiR-193b-3p-ERBB4 axis regulates psoriasis pathogenesis via modulating cellular proliferation and inflammatory-mediator production of keratinocytes, *Cell Death Dis.* 12 (2021) 963.
- [57] Y. Chen, K. Xue, X. Zhang, Z. Zheng, K. Liu, Exosomes derived from mature chondrocytes facilitate subcutaneous stable ectopic chondrogenesis of cartilage progenitor cells, *Stem Cell Res. Ther.* 9 (2018) 318.
- [58] W. Wang, X. Liang, K. Zheng, G. Ge, X. Chen, Y. Xu, J. Bai, G. Pan, D. Geng, Horizon of exosome-mediated bone tissue regeneration: the all-rounder role in biomaterial engineering, *Mater Today Bio* 16 (2022), 100355.
- [59] Y. Su, Q. Gao, R. Deng, L. Zeng, J. Guo, B. Ye, J. Yu, X. Guo, Aptamer engineering exosomes loaded on biomimetic periosteum to promote angiogenesis and bone regeneration by targeting injured nerves via JNK3 MAPK pathway, *Mater Today Bio* 16 (2022), 100434.